

Condensation/Evaporation Transition of Water in Spherical Pores in Equilibrium with Saturated Bulk Water

Ivan Brovchenko* and Alla Oleinikova

Physical Chemistry, Dortmund University of Technology, Otto-Hahn-Str. 6, Dortmund, D-44227, Germany

Received: August 26, 2010; Revised Manuscript Received: October 16, 2010

Liquid–vapor phase transition of water in spherical pores with various strengths of water–surface interaction is studied under conditions of equilibrium with the saturated bulk water. The excess chemical potential of bulk liquid water along the liquid–vapor coexistence curve was determined by the overlapping distribution method. The adsorption and desorption of water in pores were studied by Monte Carlo simulations in the grand canonical ensemble in the temperature range $T = 270\text{--}580\text{ K}$ with a step 10 K . The well depth U_0 of the water–surface potential was varied from $\approx -0.6\text{ kcal/mol}$ (hydrophobic pore surface) to $\approx -7.1\text{ kcal/mol}$ (hydrophilic pore surface). The diagram showing the areas of the stable, metastable, and unstable liquid and vapor phases of confined water in the $T - U_0$ plane has been constructed. Water vapor only exists in pores with $U_0 > -1.2\text{ kcal/mol}$, whereas liquid water only exists in pores with $U_0 < -2.8\text{ kcal/mol}$. The interval ΔU_0 , where both stable and metastable states of confined water are possible, shrinks upon heating almost linearly and disappears at the hysteresis pore critical temperature T_p^h . Above T_p^h , there is a particular value $U_0^* \approx -1.35\text{ kcal/mol}$ that divides the regimes of capillary condensation and capillary evaporation up to the pore critical temperature T_p . The obtained results can be used for the optimization of porous materials for applications that require controlled adsorption and desorption of water.

Introduction

The adsorption/desorption of water in porous materials plays an important role in various technological applications. In particular, it can be used for the storage of heat and cold. The dry porous material is a battery with stored heat, which can be released in the right time by exposing this material to water vapor (available in air or in technological processes).^{1,2} The drying (recharging) of the porous material can be achieved by its heating when exposed to undersaturated vapor in the time when the source of cheap heat is available (solar heat during the day, waste heat in power and other plants, etc).

The efficiency of the existing systems for heat storage based on the adsorption/desorption of water in porous materials is rather low, which makes them expensive and limits their practical use. The adsorption of water below the monolayer coverage at strongly hydrophilic pore surface of zeolites or silica gels is used for heat storage in the available devices. The advantage of this method is the high heat of adsorption that provides the efficient adsorption of water even at conditions of low humidity. The disadvantage of this method is the low water uptake as only hydration water is involved in cyclic process. Another serious disadvantage is related to the fact that the adsorption/desorption of water in such system is related to some phase transition, which is strongly smeared out in the temperature and pressure ranges. In nanopores (zeolites), this is a “bulk” liquid–vapor transition of water, smeared out by the small system size. In larger pores (silica gels), this is a condensation of surface water (layering transition) smeared out due to the heterogeneity of the pore surface and due to relatively low values of the critical temperature of the layering transition. As a result, the adsorption/desorption occurs gradually with

temperature thus requiring strong temperature changes for desirable heat storage density.

High water uptake and, accordingly, high heat storage density can be achieved when the latent heat of the liquid–vapor transition of water in meso- and micropores is used for storage. In porous materials with uniform pore sizes, this liquid–vapor transition can occur at some particular values of temperature and chemical potential of the external bulk water, which are determined by the pore properties. Therefore, the efficient use of the liquid–vapor transition of water in porous materials requires optimization of the pore materials for each particular technological process. For example, high temperatures (above $100\text{ }^\circ\text{C}$ and up to the supercritical conditions) and high levels of humidity are typical for power plants, whereas lower temperatures and usually lower humidities are typical for domestic applications. In most cases, the external bulk water is in a vapor phase and, therefore, the chemical potential of external water vapor can vary from low values corresponding to the low-pressure vapor up to the upper limit determined by the bulk liquid–vapor transition. For the purposeful optimization of the porous materials it is important to know enthalpy and mass of confined water at various temperatures and chemical potentials of the external bulk reservoir in various pores. This requires knowledge of the phase diagram of confined water, which includes the location of all phase transitions and the properties of confined water in equilibrium with the bulk reservoir being in various thermodynamic states.

The nonuniform pore size distribution of the available porous materials (especially cheap materials required for practical applications) causes the smearing out of the liquid–vapor transition of confined water in the temperature and pressure ranges, which worsens the efficiency of the heat storage. As has been proposed recently, this problem can be reduced significantly in the porous materials with variable strength of water–surface interaction^{3,4} (for example, this strength can

* Corresponding author. E-mail: ivan.brovchenko@tu-dortmund.de.

depend on temperature). If the pore surface becomes more hydrophobic upon heating, the evaporation of liquid water from such pore occurs at some particular strength of water–surface interaction. In accordance with the Kelvin equation,⁵ the shift of the liquid–vapor transition in pore in terms of pressure (chemical potential) is proportional to $\cos \theta$ (where θ is a contact angle) and inversely proportional to the pore size. Therefore, this shift is equal to zero for pores of *all* sizes if $\cos \theta = 90^\circ$. This situation corresponds to the particular strength of fluid–wall interaction, when no drying nor wetting transition occurs upon heating. Therefore, in equilibrium with the saturated bulk fluid, the condensation/evaporation transition of fluid in pores of all sizes should occur simultaneously at some particular strength U_0 of fluid–surface interaction.

The phase diagram of a fluid in a pore depends strongly on pore morphology (pore size distribution, pore shape, etc.) and on the pore surface properties (strength of water–surface interaction, surface heterogeneity, etc.).^{6–8} It includes the liquid–vapor phase transition affected by confinement, the additional phase transitions driven by the surface (layering, prewetting), and the surface transitions (wetting, drying). Although a great variety of phase diagrams is therefore possible for confined fluids, scant information is available for the phase diagrams of confined water.⁸ In experiments, it comes mainly from the measurements of the adsorption isotherms. However, these measurements are usually performed under conditions of low temperatures (below 100 °C) and low humidities. Besides, the hysteresis phenomena prevent localization of the equilibrium phase transitions. We are not aware of the phase diagrams of confined water measured experimentally.

The phase transitions of water confined in various pores have been extensively studied by simulations (see refs 7 and 8 and references therein). In some cases, the coexistence curves corresponding to the liquid–vapor and to the surface transitions of confined water have been obtained.^{9–16} The most detailed studies have been performed by simulations of water in various pores with smooth surfaces in the Gibbs ensemble.^{12–15} This gave the possibility to observe the evolution of the phase diagram of confined water with varying pore sizes and the strength of the water–surface interaction and to construct the surface diagram of water in the limit of large pores.⁸

In the simulations of confined water in equilibrium with the external bulk reservoir, the values of the chemical potential of the simulated water model along the bulk liquid–vapor coexistence are usually unknown. This prevents simulations of confined water in equilibrium with the *saturated* bulk water as with the bulk vapor of well-defined humidity. The direct equilibration of confined and bulk liquid water has been performed in the Gibbs ensemble.^{17,18} It has been found that there is some critical strength of the water–surface interaction, which divides regimes of capillary condensation and capillary evaporation. For water in spherical and cylindrical pores with radius 12 Å at $T = 300$ K, the well depth of the critical water–surface potential is about -1.5 ± 0.4 kcal/mol. Note that this estimation is very rough and it is not clear how this critical interaction changes with the temperature and with the pore size.

The main goal of the present paper is to obtain the diagram showing the state of confined water in spherical pores in equilibrium with the saturated bulk water as a function of the temperature T and of the strength U_0 of the water–surface interaction. This diagram should show the regions in the $T-U_0$ plane, where confined water exists in stable, metastable, and unstable vapor or liquid phase. Accordingly, it should show how the critical strength U_0 of the water–surface interaction, dividing

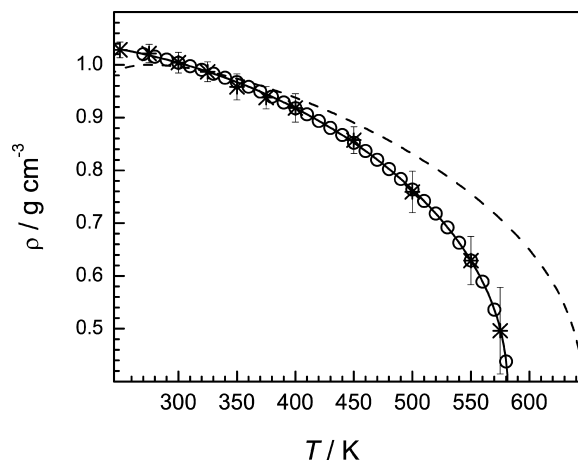


Figure 1. Density of liquid TIP4P water along the liquid–vapor coexistence curve: asterisks, state points obtained by MC simulations in the Gibbs ensemble;¹² solid line, eq 1; circles, state points simulated in the present paper; dashed line, experiment.²³

the regimes of capillary condensation and capillary evaporation, depends on temperature. Such diagram not only shows the temperature changes of water properties in pores with temperature independent strength of water–surface interaction ($U_0 = \text{const}$) but also allows prediction of the condensation/evaporation transition in pores whose U_0 varies at constant temperature and in pores with thermosensitive surfaces ($U_0 = U_0(T)$). Knowledge of such diagram opens a possibility to predict the pore parameters (first of all, U_0 and its variation) optimal for the particular technological process, thus allowing optimization of the porous materials used in the applications related to the storage of heat and cold.

Methods

Simulations of the Chemical Potential of Bulk Water. The TIP4P model with a spherical cutoff at 8.5 Å was used for water.¹⁹ The densities of bulk liquid water and water vapor along the liquid–vapor coexistence curve were obtained for this model in our previous studies by Monte Carlo (MC) simulations in the Gibbs ensemble (asterisks in Figure 1).¹² These densities were fitted to the extended scaling equation and the temperature dependence of the density ρ_l of liquid water can be described as

$$\rho_l (\text{g/cm}^3) = 0.330(1 + 1.58\tau - \tau^2) + 0.681\tau^{0.326}(1 + 0.246\tau^{0.53} - 0.51\tau^{1.04}) \quad (1)$$

where $\tau = 1 - T/T_c$, $T_c = 581.9$ K (solid line in Figure 1).

In the present studies, the bulk liquid water was simulated in the constant volume ensemble using 512 molecules with densities fixed at the values determined by eq 1. The simulations were performed in the temperature interval between 270 and 580 K with a step 10 K (circles in Figure 1). The equilibration of the systems required from 2×10^6 to 4×10^6 MC steps and the productive runs consisted of 10^8 to 1.5×10^8 MC steps. Each step corresponds to the random displacement and rotation of a randomly chosen molecules. The maximal possible displacement and rotation of a molecule were chosen at each temperature to provide the probability of the acceptance of MC step of about 30–40%.

The excess chemical potential of bulk liquid water along the liquid–vapor coexistence curve was obtained by the overlapping

distribution method.²⁰ The probability distribution $p_0(E)$ of the potential energy E of molecules in liquid water and the probability distribution $p_1(E)$ of the potential energy E of molecules randomly inserted in liquid water were calculated at all temperature studied. For this purpose, at every 500th MC step, the potential energies of all water molecules as well as the energy of the additional water molecule randomly inserted in the simulation box were calculated. The probability distribution $p_0(E)$ was obtained by about 1.3×10^8 attempts to delete a water molecule from the simulation box, and the probability distribution $p_1(E)$ was obtained by about 1.3×10^9 attempts to insert a water molecule in the simulation box. The excess chemical potential μ_{ex} of the water molecules was determined from these distributions as²⁰

$$\mu_{\text{ex}}(T) = E + k_B T \ln(p_0(E)/p_1(E)) \quad (2)$$

where k_B is a Boltzmann constant.

Model Pore. The pore was modeled as a spherical cavity of a radius $R_p = 12 \text{ \AA}$ in a solid material composed of monodisperse spherical particles. The potential energy of the interaction of water molecule with a solid material U_{ws} was represented as a sum of the LJ (6-12) potentials U_{wp} between water oxygen and i th particle separated by distance x_i :

$$U_{\text{ws}} = \sum_i U_{\text{wp}}(x_i) = \sum_i 4\epsilon[(\sigma/x_i)^{12} - (\sigma/x_i)^6] \quad (3)$$

For simple pore geometry, homogeneous distribution of particles and in continuous approximation, the interaction U_{ws} of water oxygen with a solid material is a function of its distance r to the surface only. The dependence $U_{\text{ws}}(r)$ can be obtained by the integration within some shell of a solid material. For the planar infinite surface ($R_p = \infty$), the integration over half space gives

$$U_{\text{ws}}(r) = \frac{2}{3} \epsilon n \sigma^3 \pi \left[\frac{2}{15} (\sigma/r)^9 - (\sigma/r)^3 \right] = \frac{11}{6} \epsilon n \sigma^3 \pi [(\sigma^*/r)^9 - (\sigma^*/r)^3] \quad (4)$$

where n is a numerical density of particles and $\sigma^* = (5/7)\sigma$. This potential with $\sigma = 3.5 \text{ \AA}$ has been used in extensive simulation studies of water in various pores.^{8,12–15} When the prefactor outside the latter square brackets is equal to 1, the well depth U_0 of the potential $U_{\text{ws}}(r)$ is equal to -0.385 kcal/mol .

Interaction of water with pore wall depends strongly on the pore size and shape and the potential $U_{\text{ws}}(r)$ can strongly deviate from that for planar surface ($R_p = \infty$) described by eq 4, especially in narrow pores. The potential $U_{\text{ws}}(r)$ in the spherical pores has been obtained by numerical integration of the potentials $U_{\text{wp}}(x)$ given by eq 3 with $\sigma = 3.5 \text{ \AA}$ within a spherical shell of width S of a solid material forming the pore walls. It was found that the obtained potential $U_{\text{ws}}(r)$ practically does not depend on the thickness S of the pore walls at $S \geq 20 \text{ \AA}$ (Figure 2). The well depth U_0 of the potential $U_{\text{ws}}(r)$ in a spherical pore of radius $R_p = 12 \text{ \AA}$ is about 1.54 times the value near planar surface of the same material, i.e., $U_0(R_p = \infty) = 0.65 U_0(R_p = 12 \text{ \AA})$ (see red dashed and solid lines in Figure 2). Note also the slower decay of the attractive tail of the potential $U_{\text{ws}}(r)$ in a spherical pore.

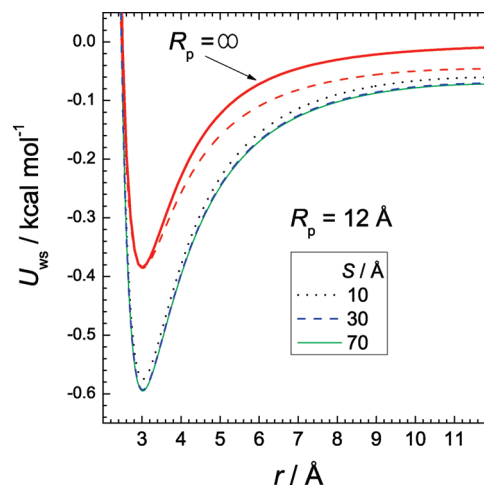


Figure 2. Potential energy U_{ws} of a water molecule in a spherical cavity of radius $R_p = 12 \text{ \AA}$ with various thicknesses S of the pore wall as a function of the distance to the pore surface r . U_{ws} near planar surface ($R_p = \infty$) and U_{ws} in pore with $R_p = 12 \text{ \AA}$ multiplied by a factor 0.65 are shown by red solid and dashed lines, respectively.

Simulations of Water in Pores. The MC simulations of water in model spherical pores were performed in the grand canonical ensemble²¹ with the value of the chemical potential fixed at the value of the saturated bulk water at the same temperature. At each temperature, the simulations were performed at various well depths U_0 of the water–pore potential from -0.6 to -7.2 kcal/mol , which corresponds to the variation of the pore surface from strongly hydrophobic to strongly hydrophilic.²² The largest step in U_0 was about 0.5 kcal/mol and it decreases to 0.05 kcal/mol in the regions of the strong changes of the pore water density. Simulations were started from empty pore for adsorption and from the pore filled with liquid water for desorption.

The type of the subsequent MC step was chosen randomly in order to provide 20% of the displacement/rotation steps, 40% of deletion steps, and 40% of insertion steps. The acceptance probability was about 30–40% for displacement/rotation steps at all temperatures. For deletion and insertion steps, in the most hydrophilic pore, the acceptance probability in the liquid phase varied from 3×10^{-4} at $T = 270 \text{ K}$ to 3×10^{-1} at $T = 580 \text{ K}$. In hydrophobic pores, these probabilities increase by at least one order of the magnitude at low temperatures. Up to 1.5×10^9 MC steps have been performed for each state point and system properties have been analyzed every 10^4 th MC step.

Results

Chemical Potential of Bulk Liquid Water. The obtained probability distributions $p_0(E)$ and $p_1(E)$ of the potential energy E of molecules in liquid water and of the potential energy E of a molecule randomly inserted in liquid water, respectively, are shown in Figure 3 at all temperatures studied. The shape of the probability distribution $p_0(E)$ is close to Gaussian. Its maximum shifts from ≈ -21.6 to $\approx -9.8 \text{ kcal/mol}$ and its half-width increases by about 35% upon heating from 270 to 580 K. The main part of the probability distribution $p_1(E)$ is located at positive values of E : the probability that a randomly inserted water molecule has negative potential energy increases from 0.2% at $T = 270 \text{ K}$ to 17.3% at $T = 580 \text{ K}$. The maximum of the probability $p_1(E)$ shifts from ≈ 14 to $\approx -0.3 \text{ kcal/mol}$ upon heating from 270 to 580 K. The shape of the probability distribution $p_1(E)$ differs notably from Gaussian. Even at low temperatures, the low-energy tail of $p_1(E)$ extends essentially

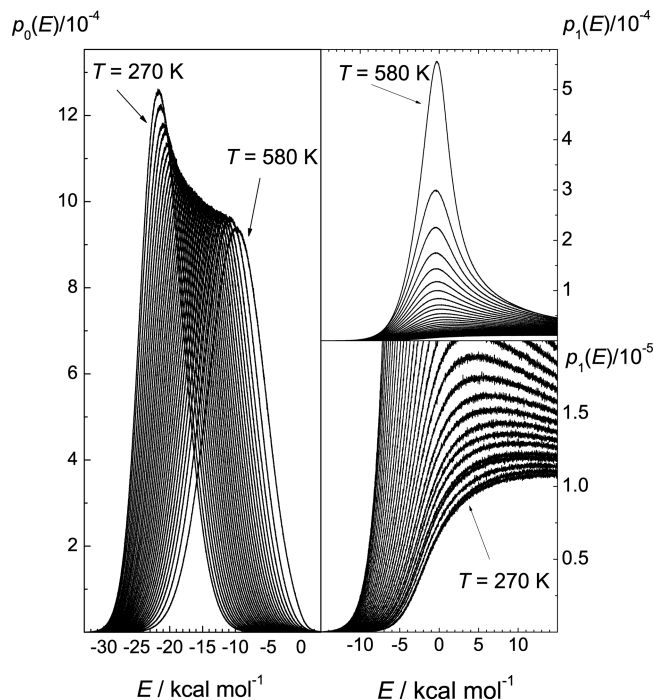


Figure 3. Probability distributions $p_0(E)$ of the potential energy E of a molecule in liquid water at all temperatures studied (left panel). The probability distributions $p_1(E)$ of the potential energy E of a molecule randomly inserted in liquid water at all temperatures studied (right panel). Lower panel shows the distributions $p_1(E)$ in the enlarged scale. The probability distributions were obtained for the step 0.01 kcal/mol.

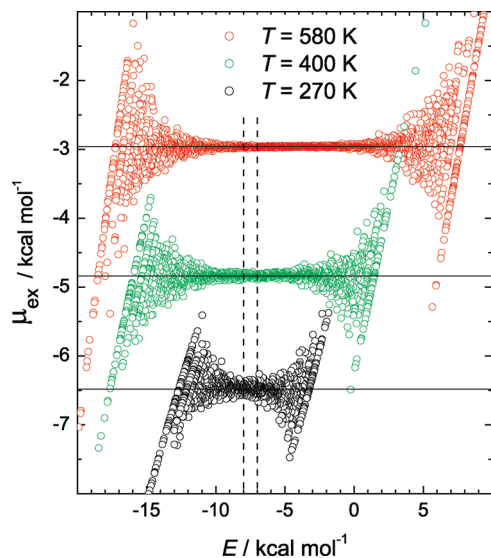


Figure 4. Excess chemical potential μ_{ex} of liquid water obtained by the overlapping distribution method using eq 1 for three representative temperatures (symbols). The average values of μ_{ex} in the interval $-8 \text{ kcal/mol} < E < -7 \text{ kcal/mol}$ (denoted by the vertical dashed lines) are shown by solid horizontal lines.

in the negative region of E (see lower panel in Figure 3), which enables an accurate determination of the chemical potential.

The values of $\mu_{\text{ex}}(T)$, calculated by eq 2, are shown in Figure 4 for three temperatures. $\mu_{\text{ex}}(T)$ were averaged in some interval of E , where the scattering of the data points in the distributions $p_0(E)$ and $p_1(E)$ was minimal. This interval is the narrowest at the lowest temperature $T = 270 \text{ K}$ and increases upon heating. The averaged values of $\mu_{\text{ex}}(T)$ are not very sensitive to the choice of the energy interval within the range $-10 \text{ kcal/mol} < E < -5 \text{ kcal/mol}$ (see upper panel in Figure 5). For certainty, we use

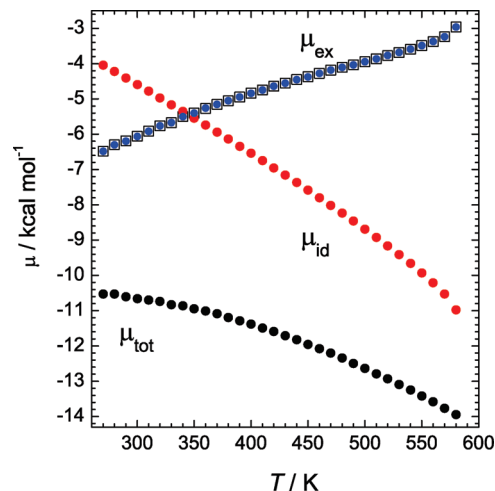


Figure 5. Excess chemical potential μ_{ex} , the ideal gas contribution μ_{id} , and their sum μ_{tot} for bulk liquid water along the liquid–vapor coexistence curve. The data points for μ_{ex} are shown for two choices of the range of E used in the calculations of $\mu_{\text{ex}}(T)$. Circles, $-8 \text{ kcal/mol} < E < -7 \text{ kcal/mol}$; squares, $-10 \text{ kcal/mol} < E < -5 \text{ kcal/mol}$.

the interval $-8 \text{ kcal/mol} < E < -7 \text{ kcal/mol}$ for calculation of $\mu_{\text{ex}}(T)$ at all temperatures studied. The total chemical potential μ_{tot} of a fluid was calculated as

$$\mu_{\text{tot}} = \mu_{\text{ex}} + \mu_{\text{id}} = \mu_{\text{ex}} + k_{\text{B}}T \ln \Lambda^3 \rho \quad (5)$$

where μ_{id} is the ideal gas contribution, Λ is the de Broglie thermal wavelength, and ρ is the fluid density. The temperature dependences of μ_{tot} , as well as of its constituents, μ_{ex} and μ_{id} , are shown in Figure 5.

Adsorption/Desorption Isotherms of Water in Pores upon Varying U_0 . The density of confined water ρ has been studied as a function of the well depth U_0 of the water–surface interaction potential at the chemical potential equal to the one of the saturated bulk water at the studied temperature. At low temperatures, confined water can stay in a liquid or in a vapor phase at the same value of U_0 depending on the initial state (see upper panel in Figure 6). As a result, the isotherms $\rho(U_0)$ show hysteresis loop within some interval of U_0 (Figure 7). At the adsorption branch of the isotherm, water remains in a vapor phase upon strengthening the water–surface interaction until some value of U_0^{max} and spontaneous condensation of vapor in pore occurs at $U_0 = U_0^{\text{min}}$ (see inset in the upper panel of Figure 7). We have determined the values of U_0^{cond} corresponding to the spontaneous condensation of water in pore (limit of stability for vapor) as an average of U_0^{max} and U_0^{min} . The values U_0^{evap} of the spontaneous evaporation of liquid water in pore (limit of stability for liquid) have been determined in a similar way from the desorption branch of the isotherm. The obtained values U_0^{cond} and U_0^{evap} are shown in Figure 8 as a function of temperature.

The width of a hysteresis loop ($U_0^{\text{evap}} - U_0^{\text{cond}}$) is 1.42 kcal/mol at $T = 270 \text{ K}$. It decreases almost linearly upon heating by 0.01 kcal/(mol K) and vanishes at $T = 420 \text{ K}$, where $U_0^{\text{evap}} = U_0^{\text{cond}} \approx -1.36 \text{ kcal/mol}$. The values of U_0^{cond} and U_0^{evap} indicating the limits of stability for vapor and liquid, respectively, linearly change upon heating: U_0^{cond} increases by $9.2 \times 10^{-3} \text{ kcal/(mol K)}$, whereas U_0^{evap} decreases by just $8.5 \times 10^{-4} \text{ kcal/(mol K)}$. Thus, the shrink of the hysteresis loop occurs mainly due to the strong temperature dependence of the limit of stability for vapor. Such analysis yields an estimation of the hysteresis pore

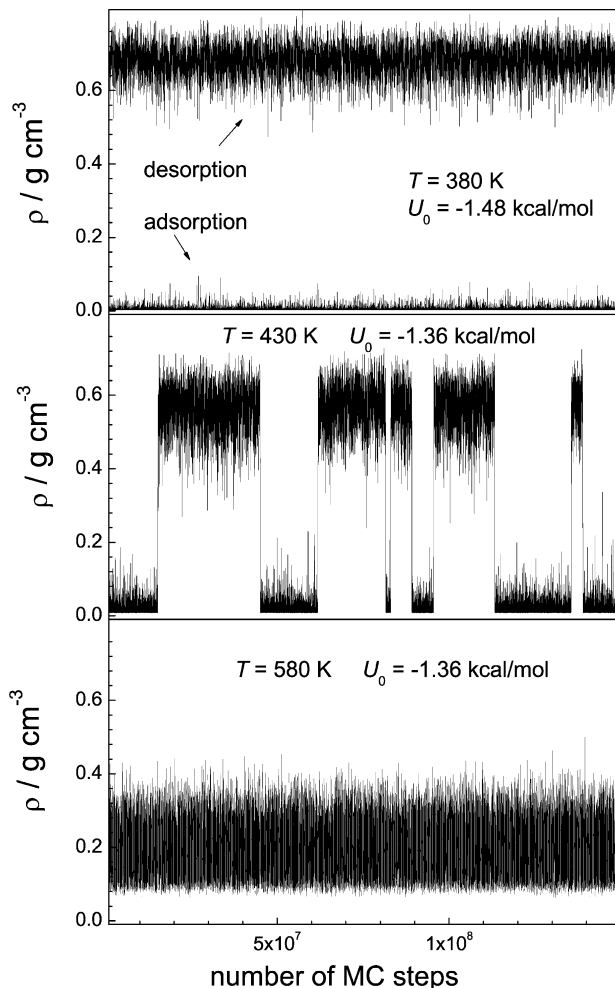


Figure 6. Variations of water density in a pore during the simulations in the grand canonical ensemble. Upper panel: below the hysteresis pore critical temperature T_c^h . Middle panel: above T_c^h , but below the pore critical temperature T_c^p at values U_0 close to that of the pore liquid–vapor transition. Lower panel: above T_c^p .

critical temperature for the pore with $U_0 \approx -1.36$ kcal/mol as $T_p^h = 415 \pm 5$ K.

At $T \geq 420$ K, the adsorption and desorption branches of the isotherm obtained by varying U_0 coincide. Note that all isotherms cross in a narrow interval of the strength of water–surface interaction between -1.31 and 1.36 kcal/mol (Figure 9). Above the hysteresis pore critical temperature, the isotherm $\rho(U_0)$ exhibits a sharp increase in a narrow interval of U_0 (see upper panel in Figure 10). In such pores, several evaporation and condensation transitions of confined water occur in the course of simulations (middle panel in Figure 6). As a result, in a narrow range of U_0 , there are strong fluctuations of water density in pores (the error bars in Figure 10 represent the standard deviations of ρ). Upon heating, the dependence $\rho(U_0)$ becomes more gradual and the density fluctuations decrease (Figure 10, middle and lower panel).

The probability distribution $P(\rho)$ of the density of confined water at $T = 430$ K is shown in Figure 11 for several values of U_0 . At $U_0 = -1.186$ kcal/mol and $U_0 = -1.423$ kcal/mol, water remains in vapor and in liquid state, respectively, during the whole simulation run. At intermediate strengths of the water–surface interaction, water exists in liquid or vapor phase during some time intervals, which appears in two distant peaks at low and high densities. Upon strengthening of the water–surface interaction, the liquid peak increases and slightly moves

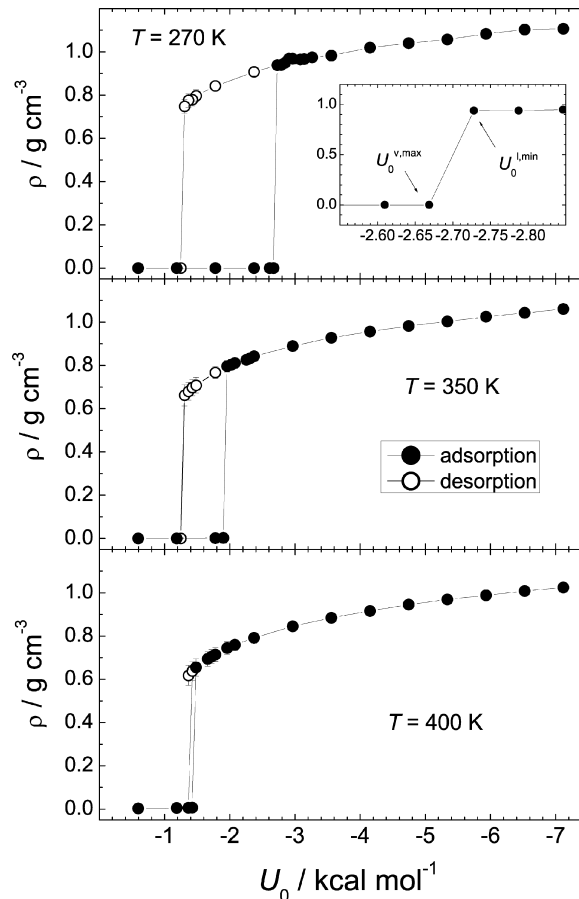


Figure 7. Density of water in pores in equilibrium with the saturated bulk for various strengths U_0 of water–surface interaction. Solid and open symbols represent simulations runs when the initial state of fluid in pore was vapor (adsorption) and liquid (desorption), respectively. Inset in upper panel shows adsorption branch in the enlarged scale.

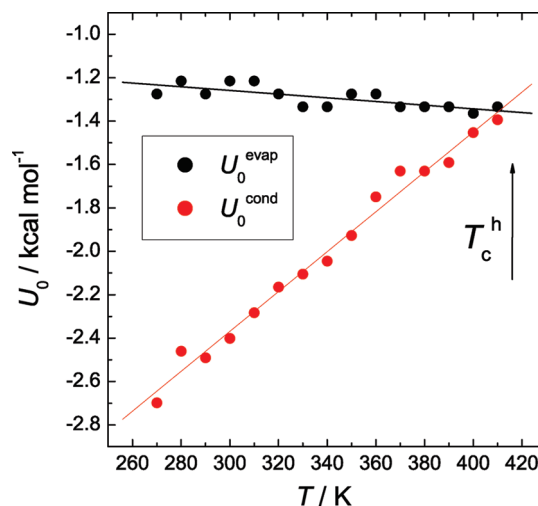


Figure 8. Temperature dependence of the stability limits for vapor (U_0^{cond}) and liquid (U_0^{evap}) phases of water in pores in equilibrium with the saturated bulk (symbols). The linear fits are shown by lines. The hysteresis pore critical temperature T_c^h is indicated by arrow.

toward higher density, whereas the vapor peak decreases. The evolution of the distribution $P(\rho)$ upon heating is shown in Figure 12 for the pore with water–surface interaction $U_0 = -1.364$ kcal/mol, providing the most pronounced two-peak structure of $P(\rho)$ at $T = 420$ K. Upon heating, two peaks of $P(\rho)$ become wider and approach each other. Two-peak structure is still seen at $T = 530$ K but disappears at $T = 540$ K.

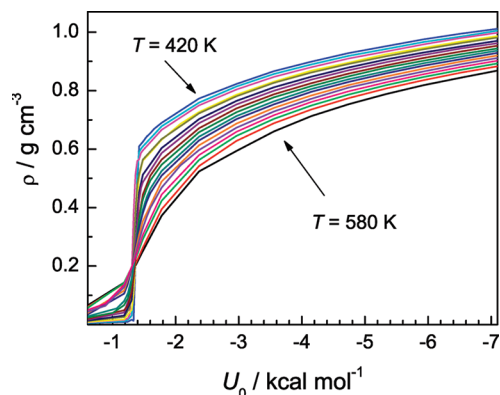


Figure 9. Density of water in pores in equilibrium with the saturated bulk for various strengths U_0 of water–surface interaction at $T \geq 420$ K.

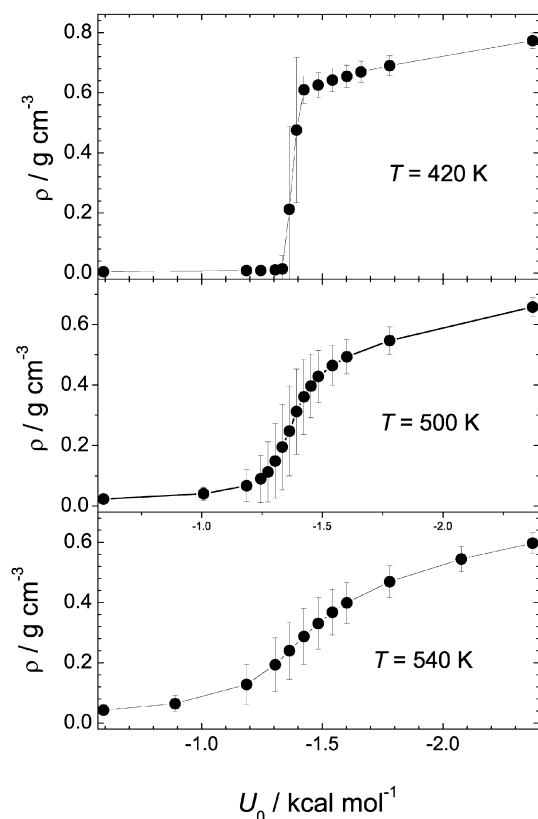


Figure 10. Density of water in pores in equilibrium with the saturated bulk for various strengths U_0 of water–surface interaction at temperatures above the hysteresis pore critical temperature T_p^h .

Therefore, the pore critical temperature for $U_0 = -1.36$ kcal/mol can be estimated as $T_p^c \approx 535 \pm 5$ K.

The probability P_1 that water exists in a liquid state was estimated by the integration of the probability distribution $P(\rho)$ for $\rho > \rho_{\min}$, where ρ_{\min} corresponds to the minimum between two peaks. This minimum is clearly seen in the logarithmic scale for probability and ρ_{\min} was found to be slightly dependent on temperature. Such analysis can be performed only for $P(\rho)$ exhibiting two-peak structure, i.e., at $T \leq 530$ K. The values of P_1 obtained in such a way are shown in Figure 13 as a function of U_0 . For the temperatures between 420 and 500 K, the dependences $P_1(U_0)$ are close to sigmoid and their widths are similar. At $T \geq 510$ K, $P_1(U_0)$ becomes essentially wider and its midpoint at $P_1 = 0.5$ shifts to the lower densities.

To describe these changes numerically, we have fitted $P_1(U_0)$ to sigmoid function, characterized by the midpoint U_0^m and the

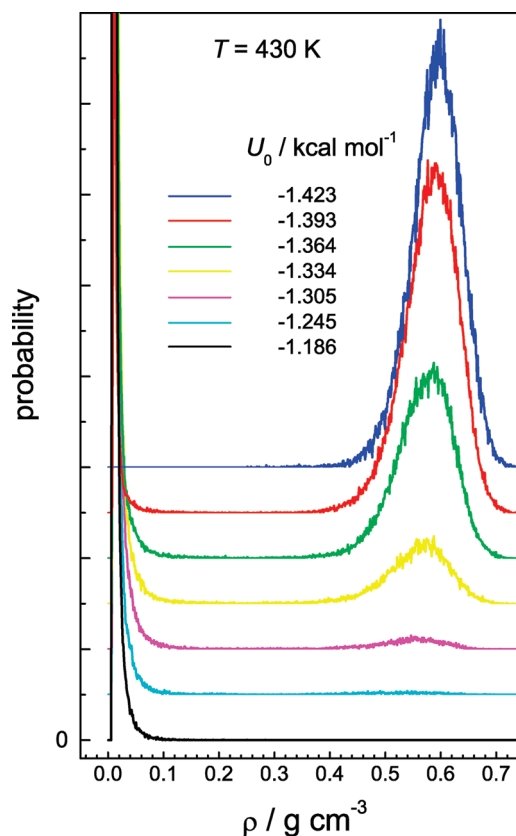


Figure 11. Probability distributions of water density in pores in equilibrium with the saturated bulk for various strengths U_0 of water–surface interaction at $T = 430$ K.

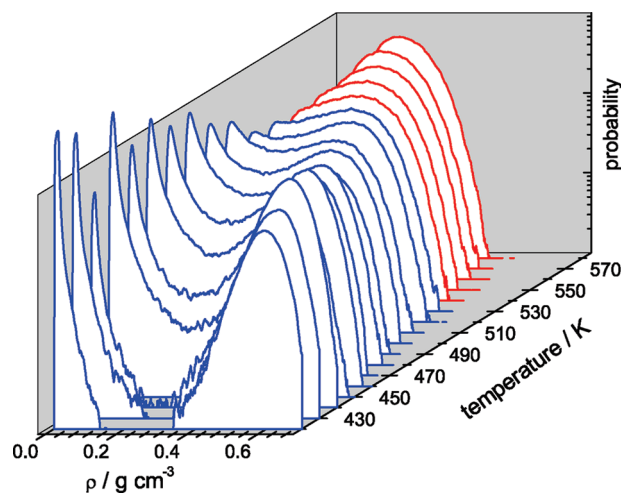


Figure 12. Probability distributions of water density in pores with $U_0 = -1.364$ kcal/mol in equilibrium with the saturated bulk water at various temperatures. Two-peak and one-peak distributions are shown by blue and red colors, respectively.

width ΔU_0 . The midpoints U_0^m of the dependences $P_1(U_0)$ shown in Figure 13 can be considered as a critical water–surface interaction U_0^c corresponding to the liquid–vapor transition of confined water. The obtained temperature dependence of U_0^m is shown in the upper panel of Figure 14. The data points show scattering in a very narrow interval of U_0 , indicating that U_0^c is practically temperature independent. The averaging of the values of U_0^m in the temperature interval between 420 and 530 K gives $U_0^c = -1.367 \pm 0.018$ kcal/mol. The temperature dependence of the width ΔU_0 of the dependence $P_1(U_0)$ shows two temperature regimes (lower panel in Figure 14). At $T \leq 500$ K,

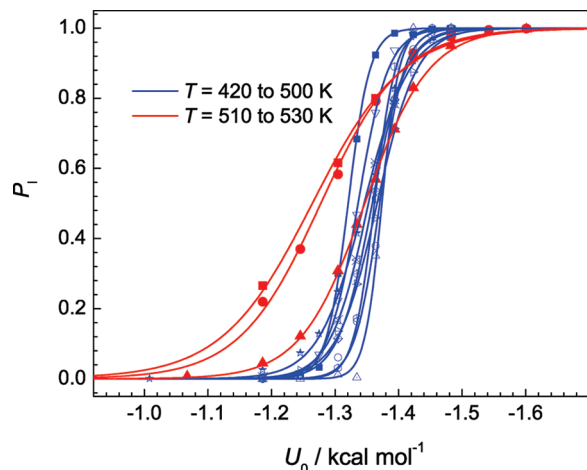


Figure 13. Probability P_1 that water exists in a liquid state as a function of U_0 for temperatures between 420 and 530 K: symbols, data points obtained from the probability distributions similar to those shown in Figure 12; lines, fits of the data points to sigmoid.

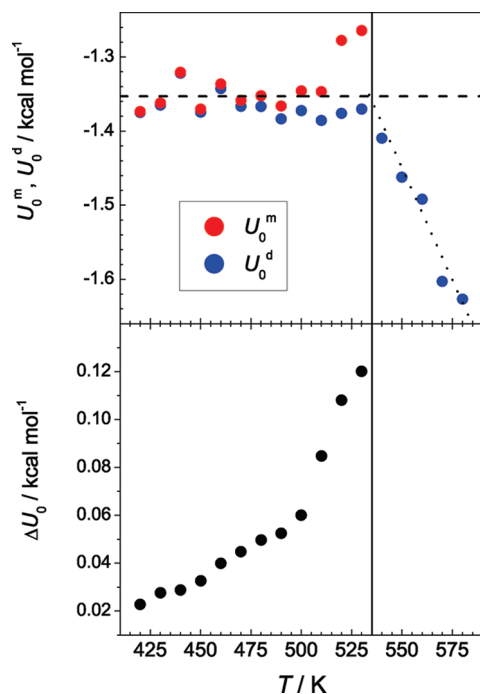


Figure 14. Temperature dependence of the midpoint U_0^m (upper panel) and width ΔU_0 (lower panel) of the dependences $P_1(U_0)$ shown in Figure 13. The temperature dependence of U_0^d corresponding to the maximum of the derivative $\partial\rho/\partial U_0$ is shown in the upper panel. The horizontal dashed line in the upper panel shows the average value (-1.353 kcal/mol) of U_0^m and U_0^d in the temperature interval from 420 to 500 K. The vertical line indicates the pore critical temperature $T_p^c = 535$ K. The dotted line is a linear fit of the values of U_0^d at $T > T_p^c$.

it increases slightly upon heating, whereas at higher temperatures it increases essentially faster. This should be attributed to the stronger smearing out of the transition in some range of U_0 with approaching the pore critical temperature due to the intrinsic finite size of the system.

The location of the liquid–vapor transitions of confined water in terms of U_0 has been also estimated by numerical differentiation of the dependences $\rho(U_0)$ and subsequent localization of the inflection point. The temperature dependence of the interaction U_0^d , where the derivative $\partial\rho/\partial U_0$ passes through a maximum, is shown in the upper panel of Figure 14. Below the pore critical temperature, the data points scatter in a narrow interval. The

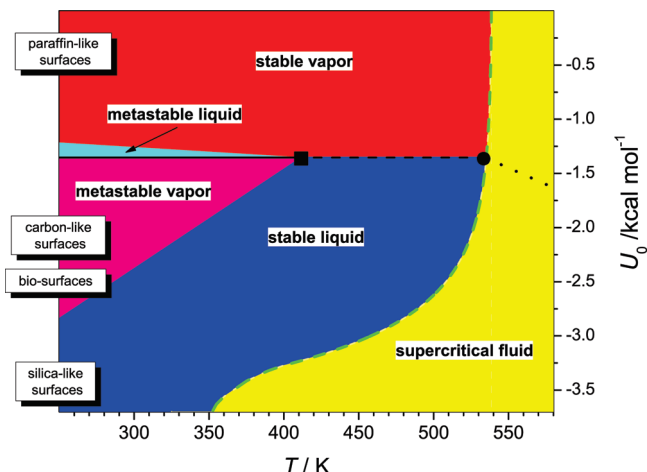


Figure 15. Diagram of confined TIP4P model water in spherical pore with radius 12 Å in equilibrium with saturated bulk water ($\mu = \mu_{\text{sat}}$) in T – U_0 coordinates. The areas of the stable and metastable vapor and liquid phases are indicated by different colors. The dashed green line is the projection of the line of the pore critical points of water in cylindrical pores with radius 12 Å at the plane T – U_0 . Yellow area corresponds to the supercritical confined water. The horizontal solid and dashed lines at $U_0^c = -1.35$ kcal/mol divide regimes of capillary evaporation and capillary condensation. The hysteresis critical temperature and the critical temperature of water in pore with $U_0 = -1.35$ kcal/mol are shown by square and circle, respectively. The dotted line in the supercritical region corresponds to the largest derivatives $\partial\rho/\partial U_0$ of confined water.

average value of U_0^d in the temperature interval between 420 and 530 K gives $U_0^d = -1.339 \pm 0.035$ kcal/mol. At lower temperatures, these points are close to those obtained from the sigmoid fit of temperature dependences of $P_1(U_0)$. Above the pore critical temperature, U_0^d deviates down from U_0^c .

Discussion

We have presented simulation studies for the phase behavior of water in spherical pores with varying strengths of water–surface interaction in equilibrium with the bulk water. The preliminary determination of the chemical potential of bulk water was required for such studies. To our knowledge, this is the first reported temperature dependence of the excess chemical potential of bulk liquid water along the liquid–vapor coexistence (Figure 5). Its value at $T = 300$ K ($\mu_{\text{ex}} = -6.06 \pm 0.04$ kcal/mol) well agrees with the several available simulation results for the chemical potential of TIP4P water at the same temperature, which vary from -5.90 to -6.11 kcal/mol.¹³ The knowledge of the chemical potential of water at saturation allows simulations at various well-determined humidities of bulk water vapor. The properties of confined water and their changes upon varying temperature depend crucially on the temperature dependence of the chemical potential of the external bulk reservoir $\mu^{\text{bulk}}(T)$. Various kinds of $\mu^{\text{bulk}}(T)$ dependences can be important in practical applications. In the present studies, we have focused only on one important (limiting) case: 100% humidity.

The diagram of the states of confined water in T – U_0 plane constructed based on the present simulation studies is shown in Figure 15. The temperature range of this diagram approximately corresponds to the interval between the temperature of the liquid density maximum (~ 250 K) and the temperature of the liquid–vapor critical point (~ 580 K) of TIP4P water.¹² Real water has about 25 °C higher temperature of the liquid density maximum and about 60 °C higher critical temperature.²³

This temperature mismatch between model and real water should be taken into account when predicting behavior of real water based on the diagram presented in Figure 15. The range of the strength of the water surface interaction U_0 varies from the paraffin-like surfaces to silica-like surfaces and approximate regions of U_0 for other surfaces are also indicated in Figure 15. The considered plane $T-U_0$ corresponds to the value of the chemical potential of water equal to its value on the bulk liquid–vapor coexistence $\mu_{\text{sat}}(T)$.

The dashed green line in the diagram shows schematically the projection of the line of the pore critical temperatures $T_p^c(U_0)$ into the $T-U_0$ plane, where $\mu = \mu_{\text{sat}}$. This line was obtained using the pore critical temperatures estimated for six cylindrical pores (with U_0 varying from -0.4 to -7.7 kcal/mol) of the same radius (12 \AA)¹³ as the radius of the spherical pores studied in the present paper. The accuracy of the determination of the pore critical temperature in cylindrical pores is about $\pm 5 \text{ K}$ for hydrophobic pores ($-0.4 \text{ kcal/mol} < U_0 < -2.0 \text{ kcal/mol}$). The sharp decrease of the pore critical temperature at $U_0 < -3.0$ kcal/mol is caused by the formation of the “dead” bilayer of water on pore surface.⁸ This bilayer is not involved in the liquid–vapor transition of water in pore that decreases an effective pore size and, accordingly, the pore critical temperature. As a result, a liquid–vapor transition occurs in a very narrow cylindrical pore with radius of about 5 \AA and the accuracy in the determination of the pore critical temperature is low ($\pm 25 \text{ K}$), when $U_0 < -2.0 \text{ kcal/mol}$. The line of the pore critical temperatures crosses the $T-U_0$ plane with $\mu = \mu_{\text{sat}}$ in one point, corresponding to the critical temperature of water in pore with $U_0^* \approx -1.35 \text{ kcal/mol}$. It deviates from the $T-U_0$ plane toward higher values of μ for more hydrophobic pores with $U_0 > U_0^*$ and toward lower values of μ for more hydrophilic pores with $U_0 < U_0^*$.

The horizontal black solid and dashed lines in the diagram correspond to the critical value $U_0^* \approx -1.353 \pm 0.031 \text{ kcal/mol}$. This value has been estimated using two methods to locate the liquid–vapor transition in the temperature interval from 420 to 530 K (see Figure 14), where there are no metastable liquid or vapor water phases in pores. At lower temperatures (below the hysteresis pore critical temperature T_p^h), there are areas in the $T-U_0$ plane where metastable liquid or vapor phases are possible. Hysteresis prevents the determination of U_0^* at $T < T_p^h$. As U_0^* is practically temperature independent at $T > T_p^h$, we can expect that this value does not change noticeably at $T < T_p^h$. The obtained value of U_0^* is within the rough estimation ($U_0^* \approx -1.5 \pm 0.4 \text{ kcal/mol}$) obtained for the same pore, when confined and bulk liquid water have been equilibrated directly in the Gibbs ensemble at $T = 300 \text{ K}$.¹⁸

The lines limiting the regions of the metastable vapor and liquid phases in Figure 15 correspond to the linear fits of the temperature dependences of their stability limits shown in Figure 8. We have found that the region of the metastable liquid phase is very narrow in terms of U_0 (blue area in Figure 15), as the value U_0^{vap} of the stability limit of a liquid is only slightly temperature dependent and is close to the equilibrium phase transition of confined water. In contrast, the stability limit for vapor measured by U_0^{cond} is strongly temperature dependent (Figure 15). This observation agrees with the theoretical and experimental results, which show that, in pores with simple geometry, the desorption branch of the isotherm is close to the equilibrium liquid–vapor transition of confined fluid and the hysteresis loop originates mainly from the metastability of the vapor phase.^{24,25} Upon heating, the changes of water density upon varying U_0 become more gradual. In the supercritical

region, the maximal variation of water density occurs when crossing the dotted line shown in Figure 15. This line corresponds to the linear fit of the values U_0^* corresponding to the maximum of the derivative $\partial\rho/\partial U_0$ (see dotted line in the upper panel of Figure 14).

The diagram in Figure 15 corresponds to the one particular pore geometry (spherical pore of radius 12 \AA). Further studies are necessary to clarify how changing the pore morphology modifies this diagram. However, some general predictions are already possible. With increasing pore size, the line of the pore critical points approaches the bulk liquid–vapor critical temperature (580 K for the considered water model) and the plane $\mu = \mu_{\text{sat}}$. It is expected that the pore hysteresis critical temperature also increases with increasing size of the pore of the same shape.^{11,26–28} Note that the area of the metastable states in $T-U_0$ plane and the value of T_p^h can be strongly sensitive to the pore morphology (pore interconnectivity, heterogeneity of pore surface, length of cylindrical pores, etc.).^{27,29} Therefore, it is difficult to predict this area for some particular pore material.

The obtained critical value U_0^* can change upon varying pore size, as the validity of the Kelvin equation worsens in narrow pores. With decreasing pore size, the values of U_0^* become more negative.¹⁷ However, the numerical estimation of this trend is not available. Rough estimations of U_0^* for cylindrical pores of the same radius give the value $\approx -1.0 \pm 0.2 \text{ kcal/mol}$.¹⁸ In large cylindrical pores of radius 25 \AA , neither wetting nor drying transitions occur at $U_0 \sim -1.0 \text{ kcal/mol}$ ^{8,15} and this value should be considered as a rough estimation of U_0^* . The simulations of water in the pores of various sizes should clarify the value U_0^* in the limit of macropores. Further development of the diagram shown in Figure 15 should include its extension along coordinate μ normal to the plane $T-U_0$. Note that in the case of $\mu \neq \mu_{\text{sat}}$, stronger size dependence of the diagram is expected.

The present simulation studies show that variation of the strength of water–surface interaction in a narrow interval of U_0 allows reversible condensation and evaporation of water in pores. The possibility to control the condensation/evaporation transition of confined water by varying U_0 is very tempting, as such control is required in various applications including storage of heat and cold. Several possibilities for the reversible varying water–surface interaction have been already reported.^{30–32} Hydrophobic films of various metal oxides³³ and conducting polymers³⁴ become hydrophilic upon light irradiation and restore their hydrophobicity in the darkness. Surfaces grafted with macromolecules undergoing conformational transition reversibly change their wettability upon varying applied electric field,³⁵ pH,³⁶ and temperature³⁷ and upon light irradiation.³⁸ The surface of copolymer changes wettability upon varying temperature due to the surface segregation of one of the component.³⁹ Strong increase of the hydrophilicity of hydrophobic surface can be achieved by adsorption of macromolecules with subsequent restoring of hydrophobic properties using detergents.⁴⁰

In the applications related to the storage of heat and cold, use of pores with *thermosensitive* surfaces undergoing hydrophilic/hydrophobic transition upon heating seems to be the most promising.^{3,4} For example, the contact angle of water at the surface grafted by poly(*N*-isopropylacrylamide) (PNIPAAm) changes from about 0° to 100° in the temperature interval between 25 and 45°C .³⁷ The modification of the inner pore surface with thermosensitive polymers has been already reported.^{41,42} In particular, silica gel synthesized with PNIPAAm shows steplike adsorption/desorption in the temperature interval where PNIPAAm undergoes temperature-induced conformational changes.⁴¹

The development of the porous materials with variable strength of water–surface interaction can drastically improve the efficiency of the devices for the storage of heat and cold. The purposeful development of such materials requires the knowledge of the thermodynamic properties of confined water in a wide range of thermodynamic states of external bulk water in pores with various strengths of water–surface interaction. The results of our studies, summarized in Figure 15, should help to choose the desirable range of the hydrophobicity/hydrophilicity of the porous materials optimal for the controlled evaporation/condensation of water in particular applications.

Acknowledgment. Financial support from the Deutsche Forschungsgemeinschaft is gratefully acknowledged.

References and Notes

- (1) *Thermal Energy Storage for Sustainable Energy Consumption: Fundamentals, Case Studies and Design*; NATO Science Series II: Mathematics, Physics and Chemistry, Vol. 234; Paksoy, H., Ed.; Springer-Verlag: New York, 2007.
- (2) Mehling, H.; Cabeza, L. *Heat and cold storage with PCM: An up to date introduction into basics and applications*; Springer-Verlag GmbH: Heidelberg, Germany, 2008.
- (3) Brovchenko, I.; Oleinikova, A.; Geiger, A. Water condensation in pores for heat storage: theoretical limits and perspectives. In *Proceedings of the 23th European Symposium on Applied Thermodynamics*, Cannes, France, 2008.
- (4) Brovchenko, I.; Oleinikova, A.; Geiger, A.; Schmidt, F. Adsorber and its use in heat accumulators and heat pumps, or refrigerators; Patent DE 102006043672 A1 UPAB 20080523, 2008.
- (5) Thomson, W. *Philos. Mag.* **1871**, 42, 448.
- (6) Gelb, L.; Gubbins, K.; Radhakrishnan, R.; Sliwinski-Bartkowiak, M. *Rep. Prog. Phys.* **1999**, 62, 1573–1659.
- (7) Brovchenko, I.; Oleinikova, A. Molecular organization of gases and liquids at solid surfaces. In *Handbook of Theoretical and Computational Nanotechnology*; Rieth, M., Schommers, W., Eds.; American Scientific Publishers: Stevenson Ranch, CA, 2006; Vol. 9, Chapter 3, pp 109–206.
- (8) Brovchenko, I.; Oleinikova, A. *Interfacial and Confined Water*; Elsevier: Amsterdam, 2008.
- (9) Rivera, J.; McCabe, C.; Cummings, P. T. *Nano Lett.* **2002**, 2, 1427–1431.
- (10) Jorge, M.; Seaton, N. A. *Mol. Phys.* **2002**, 100, 3803–3815.
- (11) Striolo, A.; Gubbins, K.; Gruszkiewicz, M.; Cole, D.; Simonson, J.; Chialvo, A.; Cummings, P.; Burchell, T.; More, K. *Langmuir* **2005**, 21, 9457–9467.
- (12) Brovchenko, I.; Geiger, A.; Oleinikova, A. *Phys. Chem. Chem. Phys.* **2001**, 3, 1567–1569.
- (13) Brovchenko, I.; Geiger, A.; Oleinikova, A. *J. Chem. Phys.* **2004**, 120, 1958–1972.
- (14) Brovchenko, I.; Geiger, A.; Oleinikova, A. *J. Phys.: Condens. Matter* **2004**, 16, S5345–S5370.
- (15) Brovchenko, I.; Oleinikova, A. *J. Phys. Chem. C* **2007**, 111, 15716–15725.
- (16) Shirono, K.; Daiguji, H. *J. Phys. Chem. C* **2007**, 111, 7938–7946.
- (17) Brovchenko, I.; Paschek, D.; Geiger, A. *J. Chem. Phys.* **2000**, 113, 5026–5036.
- (18) Brovchenko, I.; Geiger, A. *J. Mol. Liq.* **2002**, 96, 195–206.
- (19) Jorgensen, W. L.; Chandrasekhar, J.; Madura, J. D.; Impey, R. W.; Klein, M. L. *J. Chem. Phys.* **1983**, 79, 926–935.
- (20) Bennett, C. J. *Comput. Phys.* **1976**, 22, 245–268.
- (21) Allen, M. P.; Tildesley, D. J. *Computer Simulation of Liquids*; Clarendon Press: Oxford, UK, 1987.
- (22) Werder, T.; Walthers, J.; Jaffe, R.; Halicioglu, T.; Koumoutsakos, P. *J. Phys. Chem. B* **2003**, 107, 1345–1352.
- (23) Wagner, W.; Pruss, A. *J. Phys. Chem. Ref. Data* **2002**, 31, 387–535.
- (24) Foster, A. *Trans. Faraday Soc.* **1932**, 28, 645–657.
- (25) Casanova, F.; Chiang, C. E.; Li, C.-P.; Roshchin, I. V.; Ruminski, A. M.; Sailor, M. J.; Schuller, I. K. *Europhys. Lett.* **2008**, 81, 26003.
- (26) Morishige, K.; Shikimi, M. *J. Chem. Phys.* **1998**, 108, 7821–7824.
- (27) Coasne, B.; Gubbins, K.; Pellenq, R.-M. *Adsorption* **2005**, 11, 289–294.
- (28) Bonnaud, P.; Coasne, B.; Pellenq, R.-M. *J. Phys.: Condens. Matter* **2010**, 22, 284110.
- (29) Wilms, D.; Winkler, A.; Virnau, P.; Binder, K. *Phys. Rev. Lett.* **2010**, 105, 045701.
- (30) Russell, T. P. *Science* **2002**, 297, 964–967.
- (31) Liu, Y.; Mu, L.; Liu, B.; Kong, J. *Chem.—Eur. J.* **2005**, 11, 2622–2631.
- (32) Zhang, J.; Han, Y. *Chem. Soc. Rev.* **2010**, 39, 676–693.
- (33) Yan, B.; Tao, J.; Pang, C.; Zheng, Z.; Shen, Z.; Huan, C. H. A.; Yu, T. *Langmuir* **2008**, 24, 10569–10571.
- (34) Xu, L.; Chen, W.; Mulchandani, A.; Yan, Y. *Angew. Chem., Int. Ed.* **2005**, 44, 6009–6012.
- (35) Lahann, J.; Mitragotri, S.; Tran, T.-N.; Kaido, H.; Sundaram, J.; Choi, I. S.; Hoffer, S.; Somorjai, G. A.; Langer, R. *Science* **2003**, 299, 371–374.
- (36) Stratakis, E.; Mateescu, A.; Barberoglou, M.; Vamvakaki, M.; Fotakis, C.; Anastasiadis, S. H. *Chem. Commun.* **2010**, 46, 4136–4138.
- (37) Liang, L.; Rieke, P.; Liu, J.; Fryxell, G.; Young, J.; Engelhard, M.; Alford, K. *Langmuir* **2000**, 16, 8016–8023.
- (38) Ichimura, K.; Oh, S.-K.; Nakagawa, M. *Science* **2000**, 288, 1624–1626.
- (39) Reihs, K.; Voetz, M. *Langmuir* **2005**, 21, 10573–10580.
- (40) Deval, J.; Umali, T. A.; Lan, E. H.; Dunn, B.; Ho, C.-M. *J. Micromech. Microeng.* **2004**, 14, 91–95.
- (41) Ichihashi, T.; Nakano, Y. *Kagaku Kogaku Ronbunshu* **2008**, 34, 471–476.
- (42) Friebe, A.; Ulbricht, M. *Macromolecules* **2009**, 42, 1838–1848.

JP108099V